Laser Direct Writing of Crystallized TiO2 by Photothermal Effect Induced by Gold Nanoparticles

Laurent Noël, Amine Khitous, Céline Molinaro, Hsiao-Wen Zan, Dominique Berling, Fabien Grasset, Olivier Soppera

ADVANCED MATERIALS TECHNOLOGIES
www.advmattechnol.de

Laser Direct Writing of Crystallized TiO_2 by Photothermal Effect Induced by Gold Nanoparticles

*Laurent Noel, Amine Khitous, Céline Molinaro, Hsiao-Wen Zan, Dominique Berling, Fabien Grasset, and Olivier Soppera**

Near-infrared (NIR) laser annealing is successfully used to crystallize TiO_2 thin films from a sol–gel solution deposited on gold nanoparticle arrays (AuNPs). The AuNPs are used as nano-heaters allowing a local temperature increase up to 500 °C in the film. The temperature reached under the laser is deduced from the presence of the anatase phase in the samples obtained by laser exposure, showing that crystallized TiO_2 can be obtained by the photothermal effect. Different analytical techniques supported this study, such as grazing X-ray diffraction (GIXRD), UV–vis, and Raman spectroscopy. The temperature increase is confirmed by a numerical model that emphasizes the role of NPs coupling in the photothermal effect. Direct laser patterning by NIR laser and in combination with Deep-UV photolithography (DUV) are demonstrated. This fabrication method opens new perspectives in applications such as photonics, photocatalysis, or biosensing.

1. Introduction

The development of semiconducting thin films represents a large and important area of research, due to their interesting optical and electrical properties.[1] Metal oxide (MO) films are indeed used in a wide range of applications, including photodetectors,[2,3] gas sensors,[4,5] biosensors,[6] or photocatalysis.[7–9] Different routes are possible to prepare MO materials, such as physical vapor deposition or atomic layer deposition, but these techniques require complex equipment, are relatively expensive, and have some limitations in terms of chemical composition and usable substrates. A possible alternative to these techniques is the use of solutions containing metal precursors and sol–gel chemistry.[10] This route has been widely studied for several decades, due to its ease of use, low cost, and high versatility. Mesoporous metal oxide films,[11] organic–inorganic hybrid materials[12] or matrices doped with magnetic nanoparticles (NPs),[13] can be obtained by this route. However, a thermal post-annealing step is usually required to obtain suitable properties. This step is time and energy-consuming and therefore, limits the use of substrates with low heat resistance (e.g., polymers, textiles, etc.). On the other hand, laser-based processes have been developed to overcome this barrier, and local irradiation can be performed to obtain semiconducting thin films. In particular, Stehlin et al. proposed a room temperature process involving deep-ultraviolet (DUV)[14] (193 nm), to condense a wide range of sol–gel materials.[15,16] Direct writing laser patterning of photoluminescent ZnO can also be achieved by DUV exposure.[17] Recently, near-infrared condensation of indium zinc oxide (IZO) has also been performed to design an H_2S sensor.[5] Near-infrared (NIR) condensation with an NIR dye added to the solution was found to be effective in converting the xerogel into a metal oxide thin film. Alessandri et al. previously reported the formation of crystallized TiO_2 using a micrometer-sized laser spot from a Raman spectroscopy system.[18] However, they did not propose optical characterizations or experiments to show the crucial impact of the laser regime on the material. Yu et al. also showed that femtosecond laser irradiation can reach temperatures high enough to induce crystallization of TiO_2.[19] Very recently, Wu et al. proposed an interesting and promising route to pattern inorganic quantum dots, exploiting the thermal instability of surface ligands.[20] Rapid Thermal Annealing (RTA)

L. Noel, A. Khitous, C. Molinaro, D. Berling, O. Soppera
CNRS, IS2M
UMR 7361
Université de Haute-Alsace
Mulhouse 68100, France
E-mail: olivier.soppera@uha.fr
L. Noel, A. Khitous, C. Molinaro, D. Berling, O. Soppera
Université de Strasbourg
Strasbourg 67000, France
H.-W. Zan
Department of Photonics
National Yang Ming Chiao Tung University
No. 1001, Ta-Hsueh Road, Hsinchu 300, Taiwan
F. Grasset
CNRS-Saint Gobain-NIMS, IRL 3629
Laboratory for Innovative Key Materials and Structures (LINK)
NIMS
Tsukuba 305-0044, Japan
F. Grasset
CNRS, ISCR UMR 6226
ScanMAT UAR 2025
Université Rennes
Rennes F-35000, France

The ORCID identification number(s) for the author(s) of this article can be found under https://doi.org/10.1002/admt.202300407

DOI: 10.1002/admt.202300407

can be used to cure larger-scale samples with good efficiency, especially when substrate absorption participates in thin film heating.[21,22] In recent works, Intense Pulsed Light (IPL) annealing has also been proposed. In this process, the combination of multiple wavelength high-power irradiations, including DUV and NIR annealing presented above, was used to prepare Indium Gallium Zinc Oxide (IGZO) thin films with improved electronic properties for example.[23]

Processes based on absorption of metal NPs have also been proposed to trigger the condensation of a semiconductor thin film.[24–26] Usually the heating is provoked by the relaxation after resonant excitation of metal NPs. In this case, since the plasmon resonance is involved, this photothermal effect is called thermoplasmonic effect. It has been the subject of intense fundamental and applied research in recent years, with significant advances in the fields of biology,[27–30] chemistry,[31] catalysis,[32] and physics.[33,34] However, this effect has rarely been used in the field of materials science. Some recent examples using Al NPs can find applications in electronics and sensing.[35,36] The main aim of this work is to demonstrate that photothermal effects by AuNPs provide a very interesting means to prepare nanocomposites coupling metal NPs with a semiconductor material. One of the interests of metal NPs versus NIR dye relies on the stability upon irradiation of metal NPs when NIR dyes rapidly bleach. In fact, besides the interest of NPs in triggering the thermal processing of MO thin films, the coupling of metallic nano-objects with semiconductor materials has attracted much interest, especially in the case of TiO_2 and gold NPs. Indeed, due to its chemical and physical properties, as well as its high abundance on earth, titanium dioxide represents an important material for photocatalytic applications.[37] Nevertheless, UV light activation is required to excite this semiconductor, and therefore, in order to extend the activation spectral range, TiO_2 can be coupled with gold NPs.[38]

In this study, thin films of TiO_2 crystallized on gold NPs were obtained by NIR laser annealing. The material obtained by laser annealing was compared with ordinary thermal annealing. We prove here that even non-resonant NIR irradiation conditions can be used to reach temperatures high enough to obtain the crystallization of TiO_2. Numerical calculations performed on TiO_2 thin films on gold NPs confirmed the possibility of reaching the required temperatures for anatase formation. The paper also demonstrated the direct laser writing (DLW) of anatase TiO_2 in less than one second, as well as the possibility of using visible light instead of NIR for laser processing. In addition, the combination of nanoscale DUV photolithography and NIR curing was demonstrated in this paper.

2. Results and Discussion

Figure 1a illustrates the process used in this work to obtain the thin film of TiO_2 on Au nanoparticles by photothermal approach. The first step consists of the preparation of a very dense monolayer of AuNPs. The SEM image of the resulting AuNPs can be seen in Figure 1d. The method chosen here to prepare the NPs is a physical method based on the thermal dewetting of a thin gold film.[39,40] The obtained AuNPs have a mean diameter of 16.5 nm, which was determined by counting them from the SEM image. The corresponding histogram is depicted in Figure 1e. The goal is to generate a high density of NPs without aggregation, which is not easily achieved from colloidal solutions. This method also allows for some tuning of the extinction spectra of the NPs, while maintaining an appropriate polydispersity. Figure 1b shows the extinction spectrum of NPs produced by this method. The extinction maximum of the NPs on the glass substrate, in the air, is located ≈530 nm. The deposition of the titanium methacrylic acid (Ti-MAA) film causes, as expected, a redshift of the spectrum, with a maximum ≈580 nm.

The effect of NIR exposure (808 nm) on the Ti-MAA film overlying AuNPs was then studied. A NIR exposure of 65 nm thick Ti-MAA film on AuNPs induces a significant redshift (Figure 1b). According to Mie's theory, this redshift can be attributed to an increase in the effective refractive index around the NPs.[41,42] As we will show later, this refractive index change can be explained by condensation reactions inside the xerogel film by photothermal effects. However, it should be noted that despite this redshift, the conditions for exciting the plasmon resonance of the AuNPs are not reached.

Figure 1c shows a typical sample after NIR curing. This sample was obtained after washing the unexposed portion by immersion in ethanol. The blue spots correspond to the exposed areas and the color change is therefore in agreement with the redshift described above. Furthermore, this experiment shows the local cross-linking of Ti-MAA precursors by laser irradiation, which is also consistent with the laser-induced temperature rise and condensation. A complete study comparing laser and thermal annealing will be detailed later.

Prior to studying the laser-annealed material, TiO_2 thin films obtained by thermal annealing on AuNPs were characterized by multiple techniques to provide reference samples and define the temperature needed to induce significant changes in the Ti-MAA thin film (**Figure 2**). As illustrated in Figure 2a, thermal annealing causes densification of the xerogel film. The physical properties of the thin films were first studied by spectroscopic ellipsometry. The film thickness decreased gradually with annealing temperature and 80% shrinkage was observed after fast thermal annealing at 500 °C, as shown in Figure 2b. At the same time, the decrease in thickness corresponds to a densification of the film, which is also illustrated by a significant increase in the refractive index from 1.60 to 2.30.[43] The increase in the refractive index of the medium around the NPs causes a redshift in the LSPR of AuNPs (Figure 2c). This graph shows a linear dependence between the LSPR shift of the composite and the annealing temperature. As explained earlier, the refractive index increases with increasing temperature due to the densification of the film. Specifically, the relationship between refractive index and annealing temperature followed a linear trend (Figure 2b), and thus explained the behavior observed in Figure 2c. These results are important and will be used later, to compare a laser and thermal annealing.

GIXRD was used to further investigate the structure of the cured film and, specifically, its crystallinity state at a given annealing temperature. No crystallization was observed at 300 °C. Crystallized TiO_2 was observed for an annealing temperature of at least 400 °C (Figure 2d). Indeed, the main diffraction plane (101) appeared at $2\theta = 25.2°$, as well as two others at 38.0° and 48.2°, which are characteristic of anatase.[43,44] At the nanoscale, Figures S1 (Supporting Information) shows the SEM image of the AuNPs covered with TiO_2 after fast thermal annealing of 65 nm Ti-MAA

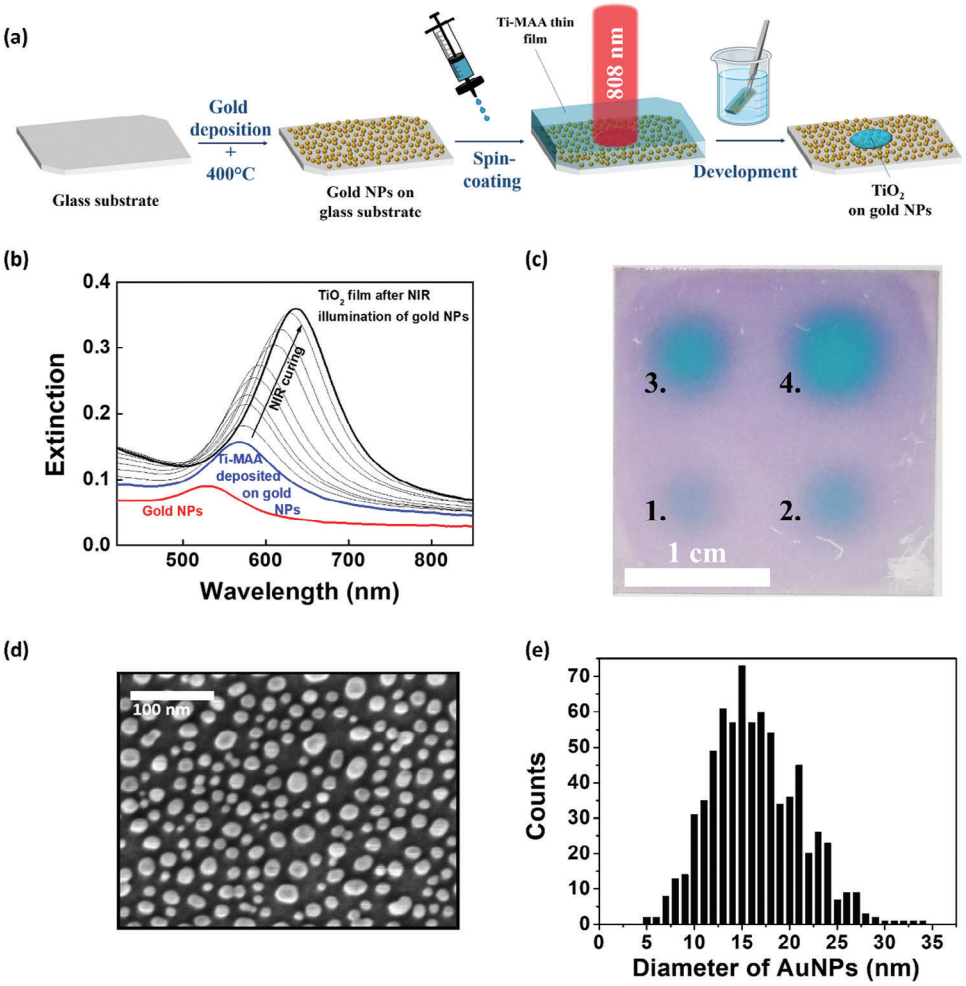

Figure 1. a) Schematic of the process to obtain crystalline TiO_2 on gold NPs by photothermal effect. b) Evolution of visible spectra with NIR energy at 1630 W cm^{-2} for gold NPs covered with 65 nm of Ti-MAA. c) Photograph of the sample obtained after a NIR exposure of 157 kJ cm^{-2} with an irradiance of (c1) 860, (c2) 1120, (c3) 1370, and (c4) 1630 W cm^{-2}. d) SEM image of gold NPs obtained after thermal dewetting of a gold thin film at 400 °C and e) the corresponding counts of gold NPs regarding their diameters.

at 500 °C. The AuNPs are no longer visible, demonstrating a complete coverage of the NPs by the TiO_2 layer. A nanoporous structure of the TiO_2 layer is observed, which could be interesting for photocatalytic applications.[45,46] XPS measurements were also performed on a spin-coated xerogel thin film (Figure S2a–c, Supporting Information) and on a TiO_2 thin film after fast thermal annealing at 500 °C (Figure S2d, Supporting Information). By comparing the O1s component of the spin-coated xerogel (Figure S2c, Supporting Information) and TiO_2 (Figure S2d, Supporting Information) thin films, we observe the removal of organic ligands which proves the mineralization (only residual organics are found due to surface contamination). Additionally, EDX analysis (Figure S3, Supporting Information) was performed on TiO_2 laser-annealed film to prove the presence of such a material.

Raman spectra (Figure 2e) confirmed a crystalline phase for the samples annealed at 400 and 500 °C. Characteristic peaks of anatase TiO_2 are observed at 153 and 647 cm^{-1}, which are attributed to the Eg mode, and at 406 and 523 cm^{-1}, for the B1g mode.[44,47,48] Another peak is also observed at 690–700 cm^{-1} at 400 and 500 °C, which is not conventional for pure crystallized TiO_2. We assume this peak could be relative to nanocrystallites for some grain size,[49] crystallite size effects,[50] or due to the embedded AuNPs in TiO_2.[51]

Since the structure of the final material may depend on the heating kinetics, this effect was also studied by Raman spectroscopy. A noticeable change in the Raman spectra was observed as a function of the heating ramp. Indeed, as shown in Figure 2f, the sample prepared by fast thermal annealing at 500 °C (Figure 2f-I) showed all the peaks characteristic of anatase TiO_2, while for the slow one (Figure 2f-II), only two main peaks at 153 and 690 cm^{-1} are distinguished. Although no significant change was observed by GIXRD analysis, an intrinsic nanoscale modification must have occurred. Discrepancies regarding the structure of thin films have already been highlighted for thermal annealing at different heating rates. Indeed, densification and crystallization are in competition depending on the heating rate. Thermal annealing at slow rates favors the formation of crystallites and porous crystals while very fast heating rates inhibit the number of crystal nuclei and promote densification.[52,53] In all cases, the presence of TiO_2 anatase can be confirmed by the main

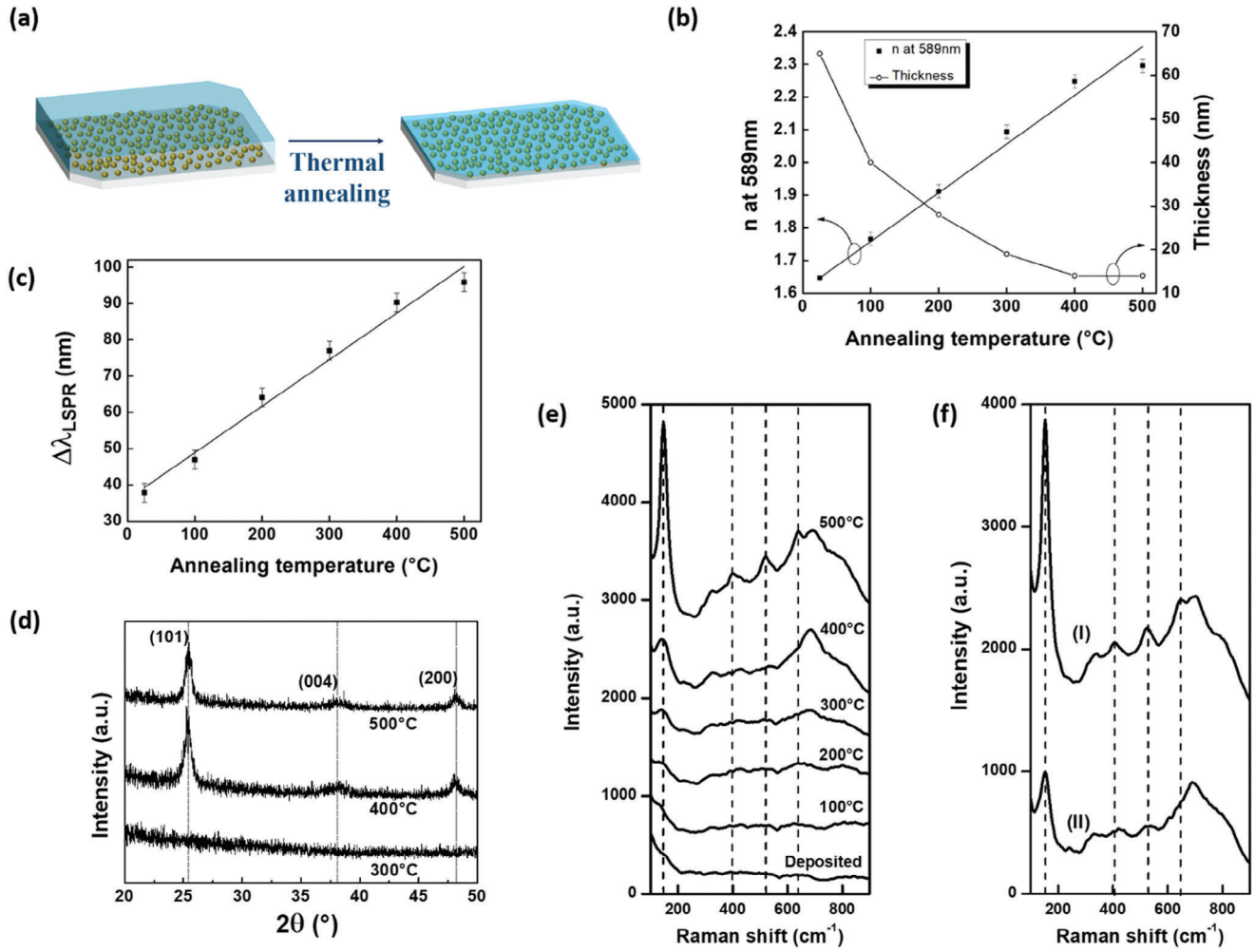

Figure 2. a) Schematic of gold NPs covered with TiO_2 thin films and thermal annealing approach. b) Thickness and refractive index of Ti-MAA thin films obtained by spectroscopic ellipsometry for different annealing temperatures. c) Evolution of the LSPR shift (in reference to NPs on the glass substrate in the air) with the annealing temperature of gold NPs covered initially with 65 nm Ti-MAA. d) GIXRD diffractograms of the TiO_2 thin films after fast thermal annealing at 300, 400, and 500°C (1 h). e) Raman spectra of gold NPs covered initially with 65 nm Ti-MAA, and thermally annealed at different temperatures. f) Comparison between the fast thermal annealing of 65 nm Ti-MAA on gold NPs at 500 °C (f-I) and the slow one, with a heating ramp of 10°C min^{-1} (f-II).

peak at 153 cm^{-1} and can therefore be used as a reference in the following.

In this section, the effect of NIR exposure (**Figure 3a**) of Ti-MAA on the AuNPs is studied and compared with thermal annealing. The Ti-MAA thin film deposited on the AuNPs is here used as a probe to study the photothermal effect generated by AuNPs upon NIR irradiation. Four different laser irradiations were used, and the condensation step was first evaluated by tracking the changes in LSPR induced by NIR irradiation. The resulting data are shown in Figure 3b. For each irradiation, a redshift of the LSPR band is observed, denoting the condensation reaction induced by the photothermal effect. The redshift increases with the dose for given irradiation, consistent with the photoinduced nature of the phenomenon.

For a given energy, the reaction yield is significantly favored for higher irradiances, showing that the photothermal effect is favored by high irradiance. Indeed, at a given energy, higher irradiances significantly favor the reaction yield, as they allow reaching higher temperatures, enhancing therefore the yield of the chemical reaction. As an example, for a dose of 157 kJ cm^{-2}, the difference in LSPR position is 50 nm between the two extreme conditions.

To compare the effect of laser irradiation with thermal annealing, the LSPR shift curve is plotted on the same graph (Figure 3b-red points) for temperatures ranging from 100 to 500 °C. It is remarkable that a larger shift of the LSPR curve can be obtained by laser irradiation at 1630 W cm^{-2}, which demonstrates the interest of laser treatment.

Raman spectroscopy analysis was used to confirm the effect of NIR irradiation. Figure 3c compares the Raman spectra of samples exposed to the same dose (157 kJ cm^{-2}) but at different irradiances. For comparison, a thermally annealed sample (500 °C, 1 h) is also shown. The sample prepared with the highest irradiance (1630 W cm^{-2}) shows a profile similar to the sample

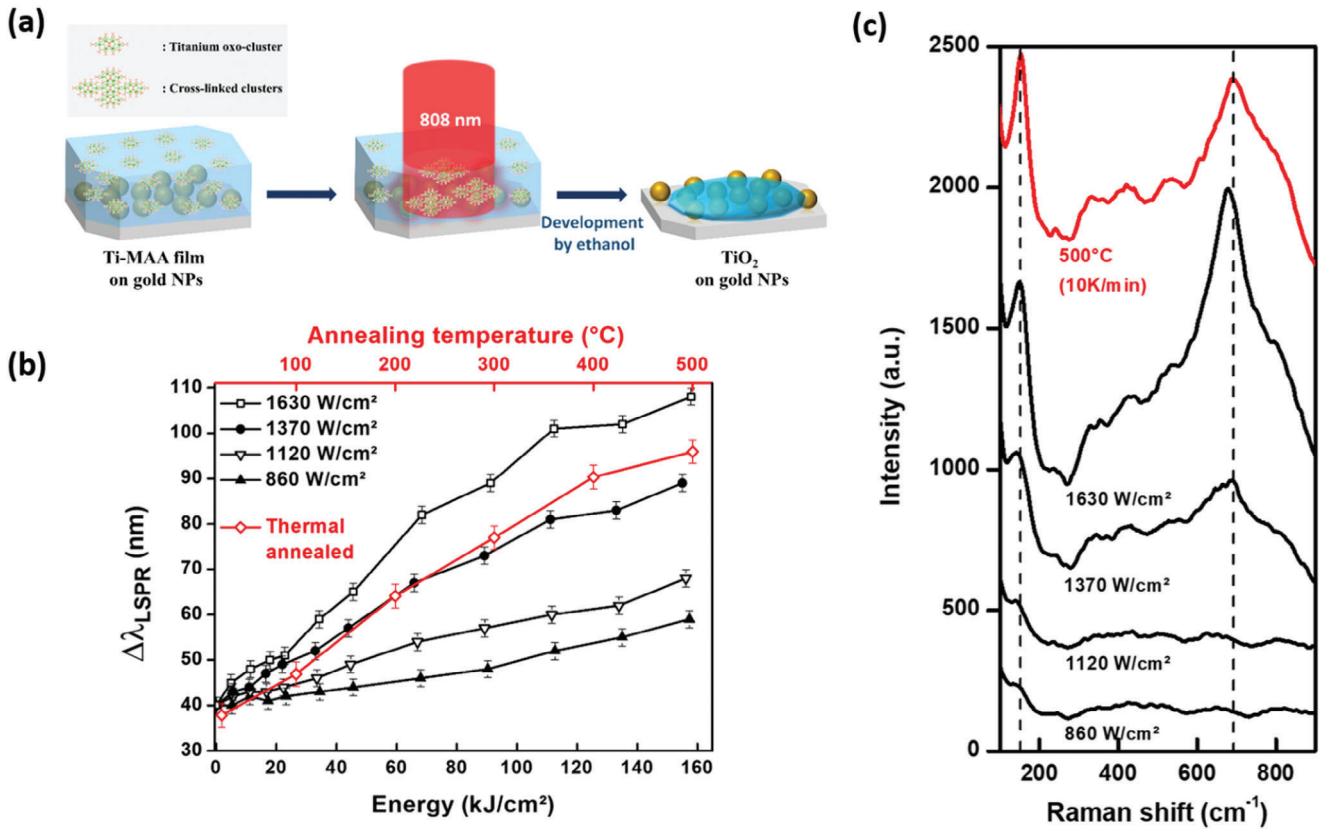

Figure 3. a) Schematic of gold NPs covered with TiO_2 after exposure of 65 nm Ti-MAA to an 808 nm continuous laser, b) evolution of the LSPR shift with the NIR energy for different irradiances and compared to fast thermal annealing and c) the resulting Raman spectra of the samples obtained at 157 kJ cm^{-2} for laser cured films and at 500 °C for the fast thermal annealed one (red color).

prepared at 500 °C. In particular, the characteristic anatase peak at 153 cm^{-1} is present and confirms the crystalline state, which clearly demonstrates that the crystalline phase of TiO_2 can be obtained at room temperature by laser treatment. Interestingly, the peak at 690–700 cm^{-1} is also present in both laser and thermal annealing conditions, confirming the similar structures in both conditions. In comparison with the evolution of the spectra shown in Figure 2c, we can conclude that the LSPR shift is indeed induced by the condensation reactions.

Partial crystallinity is also observed for the sample cured at 1370 W cm^{-2}, while for lower irradiations only amorphous phases are found. This observation is in full agreement with Figure 3b, in which the LSPR shifts at 157 kJ cm^{-2} for 860 and 1120 W cm^{-2}, are lower than those of a sample heat-annealed at 300 °C.

These results are also in agreement with GIXRD analysis (Figure 2d), which shows crystallized films at 400 °C and above. On the other hand, for the two highest laser irradiations, their equivalent temperatures are above 400 °C, and therefore the presence of anatase TiO_2 is reasonable. Moreover, the Raman spectrum for a laser irradiance of 1630 W cm^{-2} is very similar to a slow thermal annealing at 500 °C with a heating ramp of 10°C min^{-1} (Figure 2f-II).

It is interesting to compare the total irradiation time required to induce material modification with the characteristic time of thermal diffusion (τ). τ can be determined using the simple 2D thermal diffusion equation (τ = L^2/D). L is the characteristic length of the system. We chose here the full width at half maximum (FWHM) of the laser beam (L = H = 0.15 cm). *D* is the thermal diffusivity of the media. Here, *D* can be considered as the average of the diffusivities of the two-surrounding media: TiO_2 (3×10^{-6} m^2s^{-1}) and glass (0.5×10^{-7} m^2s^{-1}). In our case, the characteristic time of thermal diffusion is τ = 1.5 s. From this value, we can conclude that the thermal diffusion process is fast compared to the irradiation time. The evolution of the material during the NIR irradiation presented in Figure 3a can be thus understood as the result of the kinetics of the chemical reaction and not only the time needed to reach stationary temperature.

To confirm the experimentally obtained temperature, numerical calculations associated with temperature estimation were performed on the laser annealing system using a model described in these references.[53,54]

When multiple NPs are illuminated at the same time, the temperature increase of an NP ΔT is the sum of the temperature generated by the NP itself ΔT^s and the temperature generated by the surrounding NPs ΔT^{ext}.

$$\Delta T = \Delta T^{s} + \Delta T^{ext} \quad (1)$$

Depending on the illumination mode chosen and the size of the system, two cases are possible: either the temperature increase remains confined around each NP corresponding to

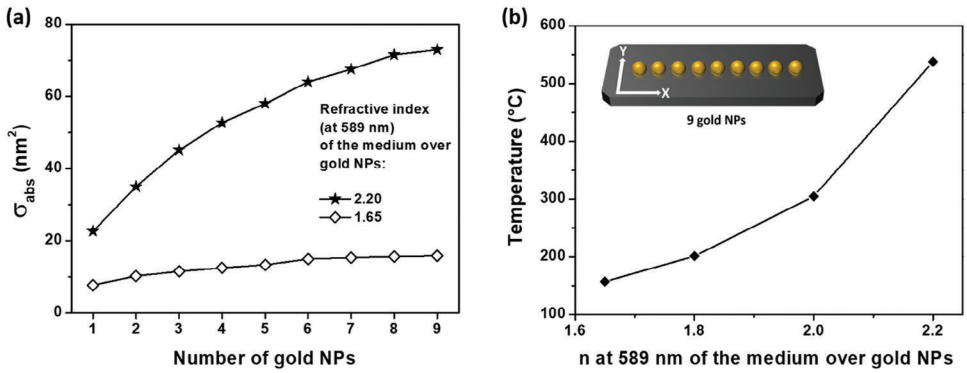

Figure 4. For a wavelength of 808 nm: a) Absorption cross-section for a gold NP with 0 to 8 surrounding gold NPs arranged in a line for different refractive indices (for n = 1.65 and n = 2.20). b) Calculated temperature during illumination for nine gold NPs depending on the refractive index over the NPs.

$\Delta T^s >> \Delta T^{ext}$, or the temperature increase is governed by the collective heating of the NPs corresponding to $\Delta T^s << \Delta T^{ext}$. The preponderance of one of these two regimes in temperature generation is represented by the parameter ζ.[55] In our case (i.e., the case of a 2D system illuminated by a Gaussian beam), ζ is defined by:

$$\zeta = \frac{\Delta T^s}{\Delta T^{ext}} = \frac{p^2}{3RH} \quad (2)$$

where p is the interparticle distance (28.8 nm), R (16.5 ± 3.5 nm) is the radius of the NP, and H is the full width at half maximum of the Gaussian beam. R and p were extracted from the SEM images of the samples processed by the Fiji software.

Here, we obtain $\zeta = 1.5 \times 10^{-5} << 1$. The temperature of the system is thus governed by the collective heating effect of the NPs inducing a relatively homogeneous and smooth temperature in the laser spot as shown in Figure 1c.

Since the temperature increase of the sample during laser illumination is governed by the collective temperature increase, it can be estimated by the following equation in the case of Gaussian illumination of an infinite array[55]:

$$\Delta T^{ext} \approx \frac{\sigma_{abs} P}{\kappa} \sqrt{\frac{\ln 2}{4\pi}} \frac{1}{HA} \left(1 - \frac{4\sqrt{\ln(2)}\, A}{\pi H}\right) \quad (3)$$

where σ_{abs} is the absorption cross-section, P is the incident illumination power, $\kappa = (\kappa_s + \kappa_m)/2$ is the mean of the thermal conductivity of the substrate (κ_s (glass) = 1.38 W m^{-1} K^{-1} or κ_s (quartz) = 1.40 W m^{-1} K^{-1}) and the surrounding medium κm, H the FWHM of the Gaussian beam and A is the unit cell area of the NP lattice.

The absorption cross-section σ_{abs} was calculated using the Matlab MNPBEM (Multiple NanoParticles Boundary Elements Method)[56] toolkit. Numerical simulations were performed with nanodisks on the glass substrate (n = 1.5) in a surrounding medium (i.e., TiO_2 matrix). The disk modeled here has a rounded edge at the top and a sharp edge at the bottom in contact with the substrate. The thickness of the disk was evaluated by AFM. An average value of 16 nm was found and used here. The absorption spectra were calculated in retarded mode.

Based on the sample shape (Figure 1d), we extracted from NPs counted the mean diameter of NPs d = 16.5 ± 3.5 nm and their mean interparticle distance of 28.8 nm. With consideration of the size of NPs compared to the interparticle distance, numerical simulations were performed taking into account the impact of the coupling effect between NPs.

Numerical simulations of the cross-section absorption of structures from a single gold nanodisk to 9 nanodisks arranged in a line were carried out in a surrounding medium with an index of 1.65 (amorphous Ti-MAA) and an index of 2.20 (crystallized TiO_2). Here the NPs size was set to its mean value (i.e., 16.5 nm). Absorption spectra were calculated from single AuNP to 9 AuNPs using an incident polarization X (i.e., along the NPs line). For each calculated spectrum, the cross-section absorption at 808 nm (i.e., corresponding to the wavelength of the laser) was extracted and displayed as a function of the number of NPs in **Figure** 4a for amorphous Ti-MAA (n = 1.65) and crystallized TiO_2 (n = 2.2).

First, we observed a significant increase in the absorption cross-section with the number of NPs added in the calculation, showing a coupling effect. This coupling effect between NPs is stronger when increasing the refractive index. The absorption cross-sections as a function of the number of NPs reach a plateau for 6 NPs for n = 1.65 and for 8 NPs for n = 2.2. These data show the importance of considering the coupling effect of NPs in our samples.

Moreover, since the absorption cross-section increases with the refractive index of the surrounding medium, the absorption cross-section and hence the photothermal effect will increase throughout the reaction. This effect is very interesting in our case because it corresponds to a self-catalyzing effect in the condensation reaction.

The temperature was evaluated in the case of the laser illumination shown in Figure 3 (H = 0.15 cm). We assume that the thermal conductivity of Ti-MAA is changing with temperature from 0.70 to 1.15 W m^{-1} K^{-1}, corresponding to the material before and after thermal annealing at 500 °C, respectively.[57] The calculated temperatures for the maximum power used and for 9 coupled NPs are displayed in Figure 4b. Here again, the temperature of the sample increases with the refractive index (i.e., the absorption cross-section being linear with the temperature increase – Equation 3). Consequently, taking the case of 9 NPs, which is the closest to the reality of our samples, the temperature reached at

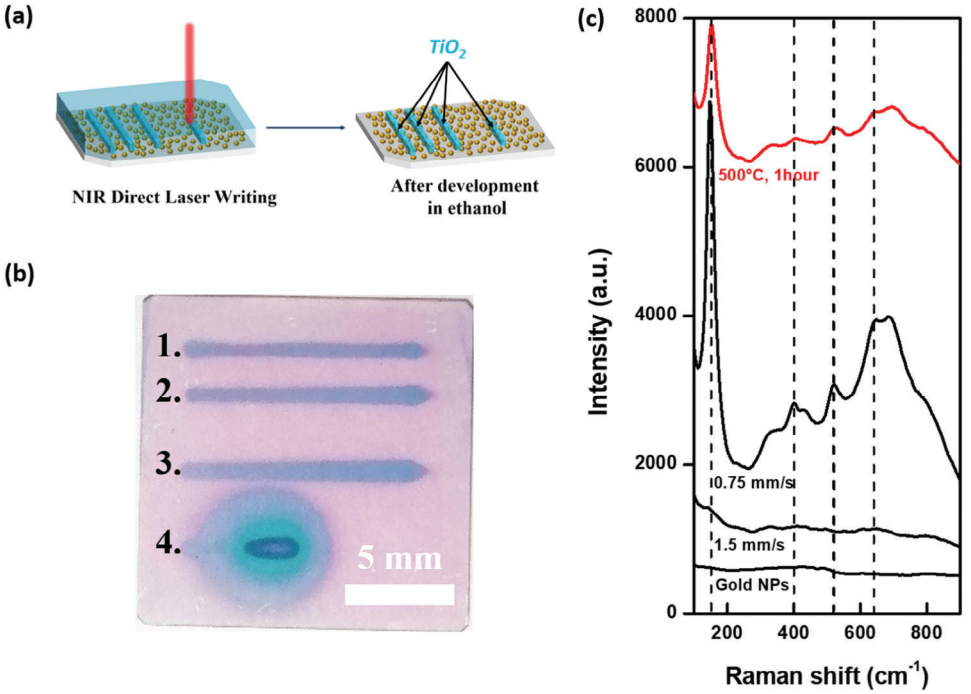

Figure 5. a) Schematic of direct laser writing process of crystalline TiO2 on gold NPs by NIR and b) a picture showing lines obtained with a writing speed of 2 mm s^{-1} at 11 kW cm^{-2} (b1) and of 2 mm s^{-1} (b2), 1.5 mm s^{-1} (b3) and 0.75 mm s^{-1} (b4) at 13 kW cm^{-2}. c) Raman spectra of gold NPs, lines (b3) and (b4), and TiO_2 obtained by fast thermal annealing at 500 °C are plotted.

the beginning of the reaction is ≈160 °C ($n = 1.65$) and at the end of the condensation ≈550 °C ($n = 2.2$). These results are in agreement with the experimentally evaluated temperature, which can go beyond 500 °C, as shown by the analysis of spectroscopic data.

We have demonstrated curing over a relatively large area (cm^2) using static irradiation with a spatially extended laser source. The efficiency of the photothermal effect paves the way for patterning by direct laser writing (DLW). **Figure 5a** illustrates this strategy to prepare arbitrary patterns of crystallized TiO_2 on AuNPs. For this purpose, the laser was focused on the sample to limit the irradiated area, and a translation stage was used to move the sample under the NIR laser beam with control of the writing speed. In this configuration, the laser beam diameter size was 600 µm. Different irradiances and writing speeds were studied (Figure 5b).

The Raman spectra of the lines produced under these conditions are shown in Figure 5c. According to the Raman spectra, lines (b1), (b2), and (b3) do not show any crystalline structure, unlike line (4) which exhibits all the characteristic peaks of anatase. Additionally, the Raman spectrum of this line has a very similar profile to that of the fast thermal annealed sample (Figure 2f-II). The difference between this direct laser writing and the static NIR exposure is mainly due to the laser power. Indeed, for the line (b4), considering a width of 0.6 mm and a writing speed of 0.75 mm s^{-1}, each point is exposed for 0.8 s for a total energy of 10.4 kJ cm^{-2}. As discussed previously for static irradiation, laser irradiance has a critical impact on LSPR shifts (Figure 3b), and for a given energy delivered, higher equivalent temperatures are achieved with higher irradiances.

One of the drawbacks of the photothermal approach is the observed lateral heat diffusion which makes it difficult to consider high-resolution patterning with such a method. To overcome this limitation, we demonstrate that we can successfully combine the NIR treatment with DUV photolithography to define patterns with better resolution. The process is described in **Figure 6a**. First, a mask was employed to obtain the logo by DUV irradiation, as shown in previous work.[15] Under DUV exposure, the modified titanium clusters undergo a photolysis of their methacrylate ligands which leads to the formation of larger clusters due to condensation reactions. Non-irradiated material is removed by development in cyclohexanone. However, the thin films obtained after DUV exposure are amorphous, and for this reason, NIR annealing is required to crystallize the material, such as previously demonstrated in this paper. After the development step, NIR annealing was only performed on "IS2M" letters to show the color change. The photos of the samples obtained at each step are shown in Figure 6b. The DUV step was done between Figure 6(b4),(b5), and NIR annealing on letters was between Figure 6(b5),(b6). A clear color change was observed on "IS2M" letters after NIR annealing. The turquoise blue indicates a much more pronounced degree of densification than for the circles just above.

In addition, Ti-MAA nanopatterns can also be obtained on AuNPs by DUV lithography and NIR annealing, such as shown in **Figure 7a**. The principle is the same as the one depicted in Figure 6, but nanostructures were obtained by DUV interference lithography instead of the millimeter-scale logo. The sample obtained after DUV exposure is shown in Figure 7b, where light is diffracted onto the patterned patches. The resulting AFM image can be seen in Figure 7c. Next, these patterns were exposed to NIR (15 s at 200 W cm^{-2}) to induce condensation reactions. The

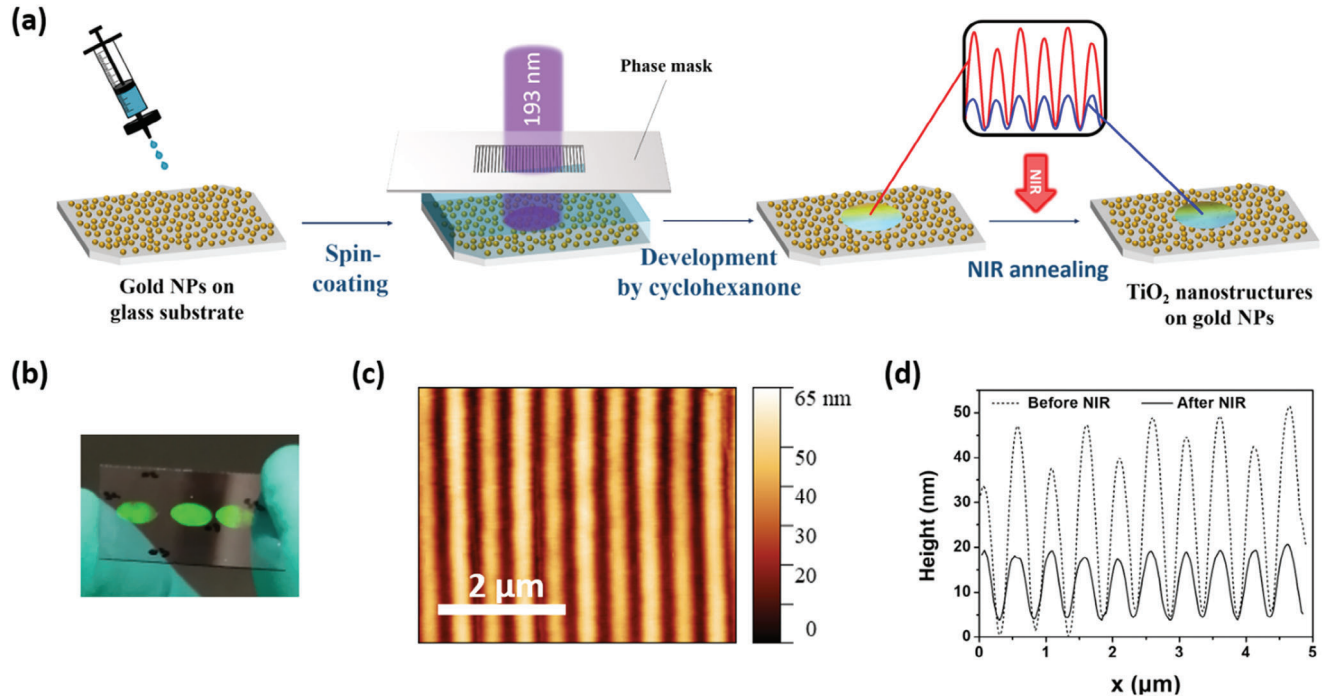

Figure 6. a) Schematic of nanostructures obtained by DUV photolithography and their curing by NIR. b) Sample with 3 spots of Ti-MAA nano-patterns obtained by DUV lithography on gold NPs and c) the corresponding AFM image for a DUV exposure of 50 mJ cm^{-2}. d) The difference in the profile of the Ti-MAA nano-patterns before and after a NIR exposure of 15 s at 200 W cm^{-2}.

difference in profile is shown in Figure 7d. The initial height of the patterns after DUV lithography was between 30 and 40 nm, while after 15 s of NIR exposure at 200 W cm^{-2}, the height dropped to 10 or 15 nm, which represents an overall shrinkage of 65%. In the end, we show through these examples that the photothermal curing by AuNPs can be applied to cure a few cm^2 of continuous thin films or patterned films.

3. Conclusion

In this study, the photothermal effect induced by NIR laser exposure on AuNPs is shown to be a very effective alternative to thermal annealing for crystallization of inorganic Ti-MAA xerogels. AuNPs have been successfully used as nano-heaters to densify and crystallize xerogel thin films by NIR (808 nm) exposure. For NIR irradiation, the formation of anatase TiO_2 was shown by LSPR peak shift and Raman spectroscopy. A comparison between thermally annealed and laser annealed samples was performed, highlighting the critical influence of laser irradiation on the final structure. Furthermore, samples exposed to very high irradiances show the same Raman spectra as those of rapidly thermally annealed samples, whereas at lower irradiances the process is more likely to be similar to slow thermal annealing. The published numerical model recovers the order of magnitude of the temperatures generated by the photothermal effect and highlights that the effect is increasingly effective during the process, due to the increase in the refractive index. The coupling between the NPs due to the high refractive index material between NPs is an important parameter that allows the treatment to be so efficient, even though plasmon resonance conditions were used. The possibility of direct laser writing was also demonstrated, as well as the possibility of combining DUV lithography and NIR curing, to generate well-defined TiO_2 patterns by laser processing at room temperature. Such a NPs/TiO_2 nanocomposite could exhibit interesting properties for SERS[58] or photocatalysis.[59]

4. Experimental Section

Materials and Chemicals: Titanium (IV) tetraisopropoxide (97%) and methacrylic acid (99%) were purchased from Merck and n-propanol from Alfa Aesar, and used as received. Silicon wafers were purchased from Siegert, glass (22 × 22 mm^2), and fused silica (15 ×15 mm^2) substrates from Carl Roth and Neyco, respectively.

Preparation of Gold NPs (AuNPs): AuNPs were obtained by thermal dewetting at 400 °C (hot plate from Harry Gestigkeit) for 1 h of a 3 nm gold film (sputtered by a CRESSINGTON 108 auto), using the same method previously published.[60] All substrates were preliminary cleaned by sonication in ethanol and acetone and placed in a UV-ozone chamber for 20 min.

Synthesis of Photosensitive Titanium Oxo-Clusters (TOC): First, a solution was prepared by mixing 0.85 g of titanium tetraisopropoxide with 2 mL of methacrylic acid (MAA) and was stirred for 5 min. Then, 2 mL of n-propanol was added to the solution and a last addition of 1 mL of deionized water (DI) was performed after 10 min of stirring. This formulation was prepared to respect molar ratios of 1:8:20 for Ti:MAA:DI. The resulting formulation was stirred for an extra hour and an aging step of 24 h was applied before use. As shown in previous studies, this formulation leads to the synthesis of nano-oxo-clusters fully covered by MAA ligands. The substitution of isopropoxide groups (—$OCH_2(CH_3)_2$) by methacrylic acid is necessary to prevent the precipitation of precursors. It also provides photosensitivity in the DUV domain used in the second part of this paper. Indeed, the presence of C═C bonds in MAA ligands improves light

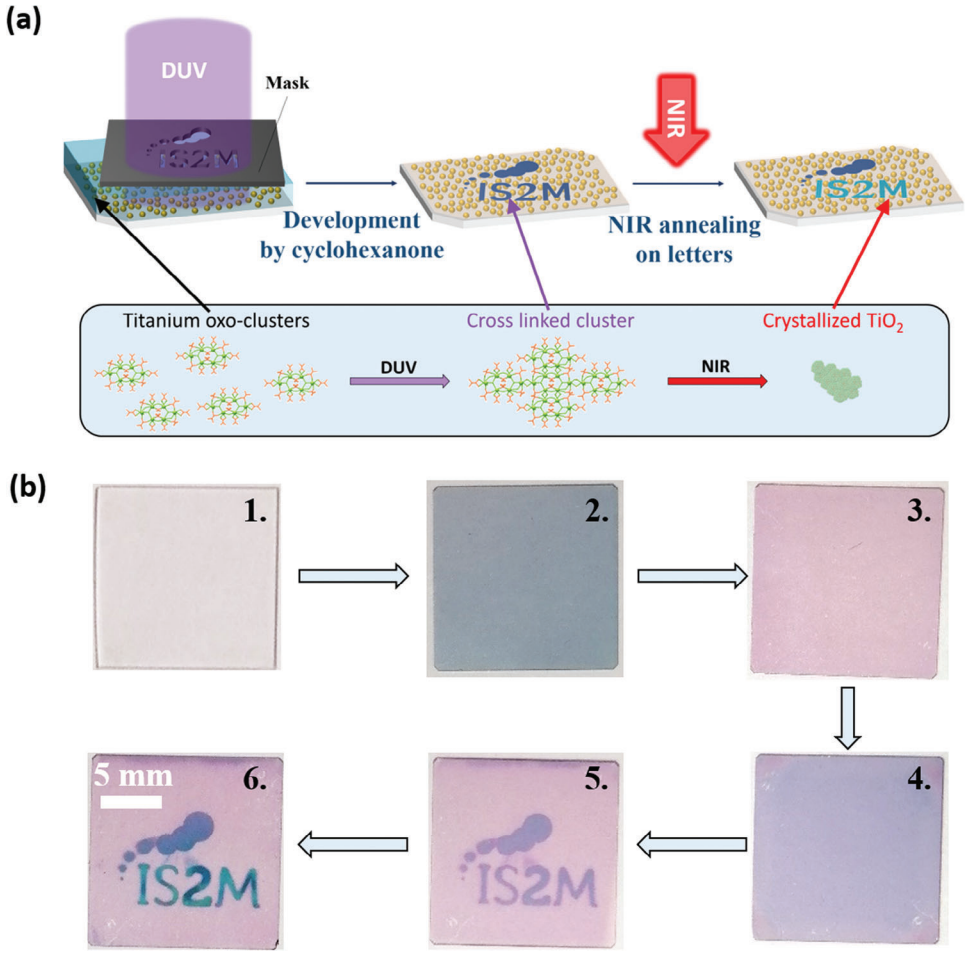

Figure 7. a) Schematic of IS2M logo obtained by DUV photolithography and direct laser writing process of crystalline TiO_2 on gold NPs by NIR. b) represents the different steps required to design the IS2M logo: fused silica (b1) is covered by a gold film (b2) and then by gold NPs obtained by thermal dewetting (b3). 65 nm of Ti-MAA was deposited onto these NPs (b4) and was irradiated by DUV through a mask (b5). The final step was the NIR exposure of the IS2M part in order to form anatase (b6).

absorption at the ArF excimer laser wavelength (193 nm), as demonstrated by Stehlin et al.[15] More details are given in the section "post-treatment of Ti-MAA films".

Protocol to Prepare Titanium-Oxide Films: In order to obtain a given film thickness, a specific volume of n-propanol was added after the 24 h aging step. In this paper, films of 65 nm were obtained for a dilution rate of 3.75, after spin-coating at 3000 rpm for 60 s, and are referred to as Ti-MAA. During the spin-coating deposition, solvent and un-complexed methacrylic acid were evaporated, leading therefore to a dense film of titanium oxo-clusters.

Post-Treatment of Ti-MAA Films: The Ti-MAA deposited films were cured following three different routes: thermal, NIR, and DUV annealing.

Thermal curing annealing was performed with an oven from Harry Gestigkeit (with a maximum temperature of 600 °C). Two different types of thermal annealing were used. The first one requires preheating the oven to the desired temperature and waiting 20 min for stabilization before placing the sample into it. This process was assigned to "fast thermal annealing" and was performed at 100, 200, 300, 400, and 500 °C. The second one, assigned to "slow thermal annealing", consists of placing the sample in the oven at room temperature (20 °C) and heating the sample to 500 °C with a heating rate of 10°C min^{-1}.

NIR curing involved a coherent-compact SE Series continuous near-infrared (808 nm) with a nominal power of 50 W. Note that this wavelength did not match the wavelength of plasmon resonance of the AuNPs covered by TiMAA, but this high-power laser source allows reaching the needed level of absorbed energy needed for the crystallization of TiO_2 as shown later. After NIR exposure, the samples were rinsed with ethanol in order to remove the unexposed area. The entire process is depicted in Figure 1a.

DUV curing was done with an excimer ArF (193 nm, Excistar from Coherent). DUV could be used to cure 1 cm^2 area or to generate nanopatterns. In this last case, a phase mask (from Ibsen photonics) with a central pitch of 1000 nm was used. The resulting patterns had a period of half the mask's pitch (i.e., a 500 nm period). The process was described in detail by Hawryluk et al.[61] Finally, to remove the unexposed parts, cyclohexanone was used as a developer.

Characterization: Thicknesses and optical coefficients of titanium-oxide based films were determined on silicon wafers by spectroscopic ellipsometry, using a UVISEL ellipsometer from Horiba–Jobin–Yvon. A simple Tauc–Lorentz model was used to fit the experimental data. UV–vis–NIR spectroscopy measurements were performed by using a white light source avalight-hal-S-mini (3 mm spot size) and an Avaspec spectrometer from Avantes. Raman spectra were obtained with a Raman BX40 visible Labram 300 from Hoshiba, at 633 nm. Grazing incidence X-ray diffraction (GIXRD) patterns of the thin films were measured on a SmartLab diffractometer (Rigaku Corp., Tokyo, Japan) with copper Kα radiation (λ = 1.5406 Å), operated at 50 mA and 40 kV. The angle of incidence (ω) was set between 0.2° and 0.8°. A Molecular Imaging Pico Plus AFM from Agilent was employed to scan sample topography (uncoated Si ACT-50 cantilever from

AppNano with a spring constant between 13 and 77 N m^{-1}). SEM images were recorded with a JSM-7900F from JEOL. X-ray photoelectron spectroscopy (XPS) measurements were performed on an XPS SES-2002 (VG SCIENTA), and the data were treated by CASAXPS.

Supporting Information

Supporting Information is available from the Wiley Online Library or from the author.

Acknowledgements

The authors would like to acknowledge the support of the Agence Nationale pour la Recherche (Projects ANR-18-CE24-0028, ANR-18-CE08-0022, and ANR-21-CE09-0035) for funding. The authors are grateful to Valérie Demange, Serge Paofaï, and Christophe Derouet from ISCR UMR6226 CNRS-UR1 for their technical assistance in GIXRD experiments performed on Osirix platform ScanMAT, UAR 2025 University of Rennes 1-CNRS. ScanMAT received financial support from the European Union through the European Regional Development Fund (ERDF), the Département d'Ille et Vilaine, Rennes Métropole, and Région Bretagne (2015–2020 CPER project SCANMAT). This work of the Interdisciplinary Thematic Institute HiFunMat, as part of the ITI 2021-2028 program of the University of Strasbourg, CNRS and Inserm, was supported by IdEx Unistra (ANR-10-IDEX-0002) and SFRI (STRAT'US project, ANR-20-SFRI-0012) under the framework of the French Investments for the Future Program. The authors thank Ludovic Josien for the SEM measurements.

Conflict of Interest

The authors declare no conflict of interest.

Data Availability Statement

The data that support the findings of this study are available from the corresponding author upon reasonable request.

Keywords

Au nanoparticles, photothermal effect, sol–gel, thermoplasmonic, TiO2

Received: March 14, 2023
Revised: October 31, 2023
Published online: November 30, 2023

[1] C.-C. Yeh, H.-W. Zan, O. Soppera, *Adv. Mater.* **2018**, *30*, 1800923.
[2] M. Patel, H.-S. Kim, J. Kim, *Adv. Electron. Mater.* **2015**, *1*, 1500232.
[3] M. Sun, Z. Xu, M. Yin, Q. Lin, L. Lu, X. Xue, X. Zhu, Y. Cui, Z. Fan, Y. Ding, L. Tian, H. Wang, X. Chen, D. Li, *Nanoscale* **2016**, *8*, 8924.
[4] H.-W. Zan, C.-H. Li, C.-C. Yeh, M.-Z. Dai, H.-F. Meng, C.-C. Tsai, *Appl. Phys. Lett.* **2011**, *98*, 253503.
[5] P.-Y. Chang, C.-F. Lin, S. El Khoury Rouphael, T.-H. Huang, C.-M. Wu, D. Berling, P.-H. Yeh, C.-J. Lu, H.-F. Meng, H.-W. Zan, O. Soppera, *ACS Appl. Mater. Interfaces* **2020**, *12*, 24984.
[6] Y. S. Rim, S.-H. Bae, H. Chen, J. L. Yang, J. Kim, A. M. Andrews, P. S. Weiss, Y. Yang, H.-R. Tseng, *ACS Nano* **2015**, *9*, 12174.
[7] A. L. Linsebigler, G. Lu, J. T. Yates, *Chem. Rev.* **1995**, *95*, 735.
[8] R. I. Bickley, T. Gonzalez-Carreno, J. S. Lees, L. Palmisano, R. J. D. Tilley, *J. Solid State Chem.* **1991**, *92*, 178.
[9] J. Sun, L. Gao, Q. Zhang, *J. Am. Ceram. Soc.* **2003**, *86*, 1677.
[10] J. Livage, M. Henry, C. Sanchez, *Prog. Solid State Chem.* **1988**, *18*, 259.
[11] A. Carretero-Genevrier, G. L. Drisko, D. Grosso, C. Boissiere, C. Sanchez, *Nanoscale* **2014**, *6*, 14025.
[12] O. Soppera, C. Croutxe'-Barghorn, D. J. Lougnot, *New J. Chem.* **2001**, *25*, 1006.
[13] C. Bidaud, D. Berling, D. Jamon, E. Gamet, S. Neveu, F. Royer, O. Soppera, *Sci. Rep.* **2021**, *11*, 5075.
[14] C.-C. Yeh, H.-C. Liu, W. Heni, D. Berling, H.-W. Zan, O. Soppera, *J. Mater. Chem. C* **2017**, *5*, 2611.
[15] F. Stehlin, F. Wieder, A. Spangenberg, J.-M. Le Meins, O. Soppera, *J. Mater. Chem. C* **2013**, *2*, 277.
[16] H.-C. Lin, F. Stehlin, O. Soppera, H.-W. Zan, C.-H. Li, F. Wieder, A. Ponche, D. Berling, B.-H. Yeh, K.-H. Wang, *Sci. Rep.* **2015**, *5*, 10490.
[17] Q. Kirscher, S. Hajjar-Garreau, F. Grasset, D. Berling, O. Soppera, *Sci. Technol. Adv. Mater.* **2022**, *23*, 535.
[18] I. Alessandri, M. Ferroni, L. E. Depero, *J. Phys. Chem. C* **2011**, *115*, 5174.
[19] S.-Y. Yu, G. Schrodj, K. Mougin, J. Dentzer, J.-P. Malval, H.-W. Zan, O. Soppera, A. Spangenberg, *Adv. Mater.* **2018**, *30*, 1805093.
[20] H. Wu, Y. Wang, J. Yu, J.-A. Pan, H. Cho, A. Gupta, I. Coropceanu, C. Zhou, J. Park, D. V. Talapin, *J. Am. Chem. Soc.* **2022**, *144*, 10495.
[21] M. C. Kao, H. Z. Chen, S. L. Young, *Thin Solid Films* **2011**, *519*, 3268.
[22] C. R. Tubío, F. Guitián, J. R. Salgueiro, A. Gil, *Mater. Lett.* **2015**, *141*, 203.
[23] C.-J. Moon, H.-S. Kim, *ACS Appl. Mater. Interfaces* **2019**, *11*, 13380.
[24] C.-F. Lin, A. Khitous, H.-W. Zan, O. Soppera, *Adv. Opt. Mater.* **2021**, *9*, 2100045.
[25] C.-F. Lin, C.-H. Chang, L. Noël, B.-R. Li, H.-F. Meng, O. Soppera, H.-W. Zan, *Adv. Mater. Technol.* **2022**, *8*, 2201026.
[26] R. Kamarudheen, G. Kumari, A. Baldi, *Nat. Commun.* **2020**, *11*, 3957.
[27] Z. Qin, J. C. Bischof, *Chem. Soc. Rev.* **2012**, *41*, 1191.
[28] N. Gupta, R. Malviya, *Biochim. Biophys. Acta, – Rev. Cancer* **2021**, *1875*, 188532.
[29] W. Yang, H. Liang, S. Ma, D. Wang, J. Huang, *Sustain. Mater. Technol.* **2019**, *22*, e00109.
[30] C. Molinaro, M. Bénéfice, A. Gorlas, V. Da Cunha, H. M. L. Robert, R. Catchpole, L. Gallais, P. Forterre, G. Baffou, *Nat. Commun.* **2022**, *13*, 5342.
[31] C. Molinaro, A. Khitous, L. Noel, O. Soppera, In *Progress in Nanophotonics 7*, (Ed.: T. Yatsui), Topics in Applied Physics, Springer International Publishing, Cham, **2022**, pp. 71–91. https://doi.org/10.1007/978-3-031-16518-4_3.
[32] J. R. Adleman, D. A. Boyd, D. G. Goodwin, D. Psaltis, *Nano Lett.* **2009**, *9*, 4417.
[33] G. Baffou, J. Polleux, H. Rigneault, S. Monneret, *J. Phys. Chem. C* **2014**, *118*, 4890.
[34] L. Cognet, S. Berciaud, D. Lasne, B. Lounis, *Anal. Chem.* **2008**, *80*, 2288.
[35] R. D. Rodriguez, S. Shchadenko, G. Murastov, A. Lipovka, M. Fatkullin, I. Petrov, T.-H. Tran, A. Khalelov, M. Saqib, N. E. Villa, V. Bogoslovskiy, Y. Wang, C.-G. Hu, A. Zinovyev, W. Sheng, J.-J. Chen, I. Amin, E. Sheremet, *Adv. Funct. Mater.* **2021**, *31*, 2008818.
[36] M. Fatkullin, R. D. Rodriguez, I. Petrov, N. E. Villa, A. Lipovka, M. Gridina, G. Murastov, A. Chernova, E. Plotnikov, A. Averkiev, D. Cheshev, O. Semyonov, F. Gubarev, K. Brazovskiy, W. Sheng, I. Amin, J. Liu, X. Jia, E. Sheremet, *Nanomaterials* **2023**, *13*, 923.
[37] R. Daghrir, P. Drogui, D. Robert, *Ind. Eng. Chem. Res.* **2013**, *52*, 3581.
[38] D. Buso, J. Pacifico, A. Martucci, P. Mulvaney, *Adv. Funct. Mater.* **2007**, *17*, 347.
[39] Sudheer, P. Mondal, V. N. Rai, A. K. Srivastava, *AIP Adv. 7*, 075303.
[40] A. B. Tesler, B. M. Maoz, Y. Feldman, A. Vaskevich, I. Rubinstein, *J. Phys. Chem. C* **2013**, *117*, 11337.
[41] C. Novo, A. M. Funston, I. Pastoriza-Santos, L. M. Liz-Marzán, P. Mulvaney, *J. Phys. Chem. C* **2008**, *112*, 3.

[42] S. Underwood, P. Mulvaney, *Langmuir* **1994**, *10*, 3427.
[43] V. V. Yakovlev, G. Scarel, C. R. Aita, S. Mochizuki, *Appl. Phys. Lett.* **2000**, *76*, 1107.
[44] D. A. H. Hanaor, C. C. Sorrell, *J. Mater. Sci.* **2011**, *46*, 855.
[45] H. Wang, T. You, W. Shi, J. Li, L. Guo, *J. Phys. Chem. C* **2012**, *116*, 6490.
[46] D. Zhou, Y. Liu, W. Zhang, W. Liang, F. Yang, *Thin Solid Films* **2017**, *636*, 490.
[47] M. Gotic, M. Ivanda, S. Popovic, S. Music, A. Sekulic, A. Turkovic, K. Furic, *J. Raman Spectrosc.* **1997**, *28*, 555..
[48] T. Ohsaka, F. Izumi, Y. Fujiki, *J. Raman Spectrosc.* **1978**, *7*, 321.
[49] C. A. Melendres, A. Narayanasamy, V. A. Maroni, R. W. Siegel, *J. Mater. Res.* **1989**, *4*, 1246.
[50] W. Ma, Z. Lu, M. Zhang, *Appl. Phys. A* **1998**, *66*, 621.
[51] A. Brognara, B. R. Bricchi, L. William, O. Brinza, M. Konstantakopoulou, A. L. Bassi, M. Ghidelli, N. Lidgi-Guigui, *Small* **2022**, *18*, 2201088.
[52] J. L. Keddie, E. P. Giannelis, *J. Am. Ceram. Soc.* **2005**, *74*, 2669.
[53] J. L. Keddie, P. V. Braun, E. P. Giannelis, *J. Am. Ceram. Soc.* **1994**, *77*, 1592.
[54] A. O. Govorov, W. Zhang, T. Skeini, H. Richardson, J. Lee, N. A. Kotov, *Nanoscale Res. Lett.* **2006**, *1*, 84.
[55] G. Baffou, P. Berto, E. Bermúdez Ureña, R. Quidant, S. Monneret, J. Polleux, H. Rigneault, *ACS Nano* **2013**, *7*, 6478.
[56] J. Waxenegger, A. Trügler, U. Hohenester, *Comput. Phys. Commun.* **2015**, *193*, 138.
[57] J. Mun, S. W. Kim, R. Kato, I. Hatta, S. H. Lee, K. H. Kang, *Thermochim. Acta* **2007**, *455*, 55.
[58] J. Lin, J. Yu, O. U. Akakuru, X. Wang, B. Yuan, T. Chen, L. Guo, A. Wu, *Chem. Sci.* **2020**, *11*, 9414.
[59] Q. Guo, C. Zhou, Z. Ma, X. Yang, *Adv. Mater.* **2019**, *31*, 1901997.
[60] A. Khitous, C.-F. Lin, F. Kameche, H.-W. Zan, J.-P. Malval, D. Berling, O. Soppera, *ACS Appl. Nano Mater.* **2021**, *4*, 8770.
[61] A. M. Hawryluk, R. M. Osgood, D. J. Ehrlich, H. I. Smith, *Opt. Lett.* **1982**, *7*, 402.